


Simulation of Catastrophic Failure in a Residual Stress Field

Sayako Hirobe^{1,*}, Kenji Imakita,² Haruo Aizawa,² Yasumasa Kato,³ Shingo Urata^{1,3} and Kenji Oguni^{1,†}

¹Research Institute for Value-Added Information Generation, Japan Agency for Marine-Earth Science and Technology, Yokohama, Kanagawa 236-0001, Japan

²Materials Integration Laboratories, AGC Inc., Yokohama, Kanagawa 221-0863, Japan

³Innovative Technology Laboratories, AGC Inc., Yokohama, Kanagawa 230-0045, Japan

 (Received 8 January 2021; revised 20 May 2021; accepted 17 June 2021; published 3 August 2021)

Residual stress has been empirically utilized for industrial applications to control material strength and shape of fragments. The interaction between the dynamically growing cracks and the residual stress field is sufficiently complicated to prevent us from building effective models. To rigorously evaluate the release and redistribution of residual stress in the dynamic fracture process, we develop a mathematical model and a numerical analysis method for the dynamic fracture in a residual stress field. Our methodology is simple and rigorous and applicable regardless of materials and scales.

DOI: [10.1103/PhysRevLett.127.064301](https://doi.org/10.1103/PhysRevLett.127.064301)

Control of the residual stress field is a significant problem in industrial applications because the residual stress field is highly related to the strength of the bulk materials. The tensile residual stress produces a stress concentration at crack tips and promotes failure. Especially under high tensile residual stress, the crack rapidly propagates and causes catastrophic fragmentation of materials [1,2]. However, the intentional introduction of surface compressive residual stress by surface machining or a finishing process [3,4] prevents crack initiation and growth. So far, because the understanding of this fracture behavior in a residual stress field is only intuitive, the controlled residual stress field is empirically employed in manufacturing techniques to improve material strength.

Fracture behavior in a residual stress field has also attracted scientific attention. However, dynamic fracture in a residual stress field brings substantial theoretical complexity because we have to solve the mutual interaction among crack propagation, change in the residual stress field, and generation of the elastic wave [5]. Moreover, although the systems and devices for the full-field measurement of the stress field have been developed in recent years [e.g., digital image correlation (DIC) [6–8] and high-speed digital photoelasticity [9–13]], these experimental approaches are limited to the evaluation of the outer surface residual stress field (DIC) or the residual stress intensity averaged over the thickness of the specimen (photoelasticity).

In view of this situation, attempts have been made toward numerical analysis of crack growth in various materials with a residual stress field [14–17]. In spite of these attempts, the achievements of previous work are mainly confined to the evaluation of the quasistatic propagation of a single crack. The dynamic propagation of multiple cracks in a residual stress field is still unsolved and highly challenging.

Mathematical model.—We first develop the mathematical model and numerical analysis method for the dynamic fracture in a residual stress field by applying the discretization scheme proposed in the particle discretization scheme finite element method (PDS-FEM) to the solid continuum with a residual stress field [18–20]. We assume that the elastic deformation is the only source of the residual stress in the solid material. The total strain tensor ϵ_{ij}^t , which represents the total deformation from the initial stress-free state, and the residual stress tensor σ_{ij} are related by $\sigma_{ij} = c_{ijkl}(\epsilon_{kl}^t - \epsilon_{kl}^p)$, where c_{ijkl} is the elasticity tensor and ϵ_{kl}^p is the permanent inelastic strain tensor. In this Letter, all the strains that do not contribute to the generation of the elastic stress (i.e., residual stress) in the linear elastic material are referred to as the permanent inelastic strain ϵ_{kl}^p .

Let us consider a deformation problem for the homogeneous isotropic linearly elastic body Ω with the prescribed distribution of the inelastic strain. In PDS-FEM, the analysis domain is discretized by using a pair of conjugate geometries corresponding to a set of nodes $\{x^\alpha\}$: Voronoi tessellations and Delaunay tessellations. Here, the superscripts α and β respectively represent the variables for the α th Voronoi tessellation and the β th Delaunay tessellation. The discretized strain energy \hat{J} stored in Ω is

$$\hat{J} = \sum_{\beta=1}^M \frac{1}{2} (\epsilon_{ij}^{t\beta} - \epsilon_{ij}^{p\beta}) c_{ijkl} (\epsilon_{kl}^{t\beta} - \epsilon_{kl}^{p\beta}) \Psi^\beta, \quad (1)$$

where M is the number of Delaunay tessellations and Ψ^β is the volume of the β th Delaunay tessellation. The summation convention is employed for subscripts throughout this Letter. This discretized strain energy \hat{J} is expressed in terms of the total displacement u_i^{α} by introducing the displacement-strain relationship in

discretized form. Then, a set of nodal displacements $\{u_i^{\alpha}\}$ minimizing the discretized strain energy \hat{J} is given by the simultaneous equations (i.e., the equation of the force equilibrium) as follows:

$$\sum_{\gamma=1}^N K_{ik}^{\alpha\gamma} u_k^{\gamma} = f_i^{\alpha}, \quad (2)$$

where the superscript γ represents the variables for the γ th Voronoi tessellation, N is the number of Voronoi tessellations, and $K_{ik}^{\alpha\gamma}$ is the stiffness matrix. This stiffness matrix is identical to that for the conventional FEM of tetrahedral elements with linear interpolation functions. Here, the nodal force is written as $f_i^{\alpha} = \sum_{\beta=1}^M B_j^{\beta\alpha} c_{ijkl}^{\beta} \epsilon_{kl}^{p\beta} \Psi^{\beta}$, where $B_j^{\beta\alpha}$ is the displacement-strain matrix. Because f_i^{α} consists of the spatial derivative operator $B_j^{\beta\alpha}$ and the inelastic strain $\epsilon_{ij}^{p\beta}$, f_i^{α} can be interpreted as the distributed internal force due to the inhomogeneous inelastic strain, which induces the residual stress [21,22].

Then, we extend Eq. (2) to the problem of the dynamic behavior of the solid continuum with a residual stress field. According to particle discretization, the solid continuum is expressed as a set of rigid body particles defined by the Voronoi tessellations. This particle expression enables the definition of the Hamiltonian for the deformable solid continuum. Here, we introduce the generalized coordinates q_i^{α} ($= u_i^{\alpha}$), the generalized velocities \dot{q}_i^{α} ($= \dot{u}_i^{\alpha}$), and the generalized momentum p_i^{α} ($= m^{\alpha} \dot{q}_i^{\alpha} = m^{\alpha} \dot{u}_i^{\alpha}$), where m^{α} is the mass of the α th Voronoi particle. The Hamiltonian H for the motion of the system of the Voronoi particles with a residual stress field is given by the sum of the kinetic energy and the potential energy of the whole body Ω as follows:

$$H = \sum_{\alpha=1}^N \frac{1}{2m^{\alpha}} p_i^{\alpha} p_i^{\alpha} + \sum_{\alpha=1}^N \sum_{\gamma=1}^N \frac{1}{2} K_{ij}^{\alpha\gamma} q_i^{\alpha} q_j^{\gamma} - \sum_{\alpha=1}^N f_i^{\alpha} q_i^{\alpha}. \quad (3)$$

The time evolution of the system of the Voronoi particles with a residual stress field is given by Hamiltonian equations:

$$\dot{q}_i^{\alpha} = \frac{\partial H}{\partial p_i^{\alpha}} = \frac{p_i^{\alpha}}{m^{\alpha}} = \dot{u}_i^{\alpha}, \quad (4)$$

$$\dot{p}_i^{\alpha} = -\frac{\partial H}{\partial q_i^{\alpha}} = -\sum_{\gamma=1}^N K_{ij}^{\alpha\gamma} q_j^{\gamma} + f_i^{\alpha} = -\sum_{\gamma=1}^N K_{ij}^{\alpha\gamma} u_j^{\gamma} + f_i^{\alpha}. \quad (5)$$

In these Hamiltonian equations, the effect of the inelastic strain is introduced as the nodal force f_i^{α} to the time evolution of the momentum. In the static equilibrium state, the right-hand side of Eq. (5) becomes zero.

For the fracture criterion, we employ the Griffith energy criterion [23]. In the framework of PDS-FEM, the fundamental unit for the expression of the crack surfaces is the boundary between two adjacent Voronoi particles. Therefore, the boundary between two adjacent Voronoi particles Φ^{α} and Φ^{γ} , denoted as $\partial\Phi^{\alpha\gamma}$, is fractured when $\Delta U \geq 2\Gamma S$ is satisfied. Here, ΔU is the released potential energy of the total system due to fracture of $\partial\Phi^{\alpha\gamma}$, S is the area of $\partial\Phi^{\alpha\gamma}$, and Γ is the surface energy determined on each material; the derivation of ΔU is provided in Ref. [24]. When $\partial\Phi^{\alpha\gamma}$ is fractured, the displacement-strain matrix $B_j^{\beta\alpha}$ and the stiffness matrix $K_{ij}^{\alpha\gamma}$ related to $\partial\Phi^{\alpha\gamma}$ are modified.

In the dynamic problems, this modification of the matrices is embedded in Eq. (5). In particular, the nodal force f_i^{α} becomes

$$f_i^{\alpha} = \sum_{\beta=1}^M B_j^{\beta\alpha*} c_{ijkl}^{\beta} \epsilon_{kl}^{p\beta*} \Psi^{\beta} \quad \forall \alpha, \beta, \gamma \text{ s.t. } \partial\Phi^{\alpha\gamma} \text{ in } \Psi^{\beta} \text{ is fractured.} \quad (6)$$

Here, the superscript $*$ represents the variables of partially fractured Delaunay tessellations. When the initial cracks are introduced, the nodal force f_i^{α} and the components of the stiffness matrix $K_{ij}^{\alpha\gamma}$ are modified due to the change in $B_j^{\beta\alpha}$. At this time, the right-hand side of Eq. (5) is no longer equal to zero and the solid continuum starts to exhibit dynamic behavior. Therefore, the dynamic fracture process in a residual stress field can be understood as the process of shifting to the new self-equilibrium state determined so as to satisfy the equilibrium condition of the distributed internal force in each and every local neighborhood. This is how the release and redistribution of the residual stress in the fracture process can be rigorously evaluated. The detailed formulation and numerical analysis method are provided in Ref. [24].

Experiment.—For the validation of the proposed model, we performed fracture experiments on chemically tempered glass sheets. Chemical tempering improves the strength of the glass sheet by artificially introducing a residual stress field in the manufacturing process through chemical treatment [24–27]. This residual stress field is controlled so as to be a compression in the outer surfaces and a tension in the interior of the glass plate to prevent growth of the surface flaws. The in-plane residual stress distribution is volumetric and uniform (i.e., $\sigma_{xx} = \sigma_{yy} = \text{const.}$, $\sigma_{xy} = 0$ when the thickness direction is set to be the z direction) and the out-plane normal residual stress is zero (i.e., $\sigma_{zz} = 0$). The residual stress profile in the thickness direction is characterized by the compressive residual stress at the outer surfaces (CS), the tensile residual stress at the midplane in the thickness direction (CT), and the depth of the compression layer (DOL). The fracture pattern of the

chemically tempered glass plate strongly depends on CT and DOL. We prepared thin rectangular plates of chemically tempered glass ($l_x \times l_y \times l_z = 50 \times 2.0 \times 0.70$ mm) with three types of different residual stress profiles, referred to as case I, II, and III: CT = 52 MPa and DOL = 39 μm in case I, CT = 75 MPa and DOL = 55 μm in case II, and CT = 112 MPa and DOL = 80 μm in case III. Then, the impactor was made to collide with the short side of the tempered glass plate to generate the initial crack and start a dynamic fracture. The approximate impact energy was 44 mJ. This energy was the same for all experiments. The collision of the impactor has no influence on the dynamic fracture process of the chemically tempered glass sheets because this collision does not cause catastrophic failure of the annealed glass sheets. The crack patterns of each glass plate are compared with the results of numerical analyses.

Numerical analysis.—We performed a numerical analysis simulating the fracture experiments of chemically tempered glass sheets presented in the previous section. We modeled the fracture experiments as shown in Fig. 1(a). We prepared the finite-element model with the unstructured tetrahedral mesh of the uniform element size. The number of nodes was 96 049 195 and the number of elements was 609 287 176. The average nodal distance was 9.36 μm . The residual stress profiles of the analysis models were adjusted to those of the three types of experimental samples with respect to CT and DOL [see Fig. 1(b)]. The detailed method for obtaining the residual stress profile of the analysis model

is provided in Ref. [24]. Then, we placed the initial crack at time $t = 0.0$ s and integrated the Hamiltonian equations [Eqs. (4) and (5)] for the constant time step $\Delta t = 0.5$ ns by using a symplectic integrator (SI) [28]. The traction-free boundary condition was applied to all the nodes at the surface of the analysis model. At each time step, all the Voronoi boundaries adjacent to the already fractured boundaries were examined to check if they satisfied the fracture criterion. Here, the mass density $\rho = 2500$ kg/m³, the Young's modulus $E = 74.0$ GPa, the Poisson's ratio $\nu = 0.22$, and the surface energy $\Gamma = 4.0625$ J/m³.

Comparisons of the fracture patterns between the experiments and numerical analyses with the different residual stress profiles are presented in Figs. 2(a) and 2(b). These figures show the crack patterns projected on the xy plane. Also, the fracture patterns obtained from the numerical analyses show perfect agreement with the experimental observations on every sample with different residual stress profiles; the crack does not bifurcate for case I, the crack branches only once to two or three cracks for case II, and the cracks repetitively branch and cause catastrophic failure for case III.

We measured the crack velocity in both experiments and numerical analyses [Figs. 3(a) and 3(b)]. For case I, the crack velocity transitions from about 1500 m/s to 2000 m/s, and it never exceeds 2000 m/s. However, for cases II and III, the crack velocity almost reaches or exceeds 2000 m/s. At this point, the cracks branch and

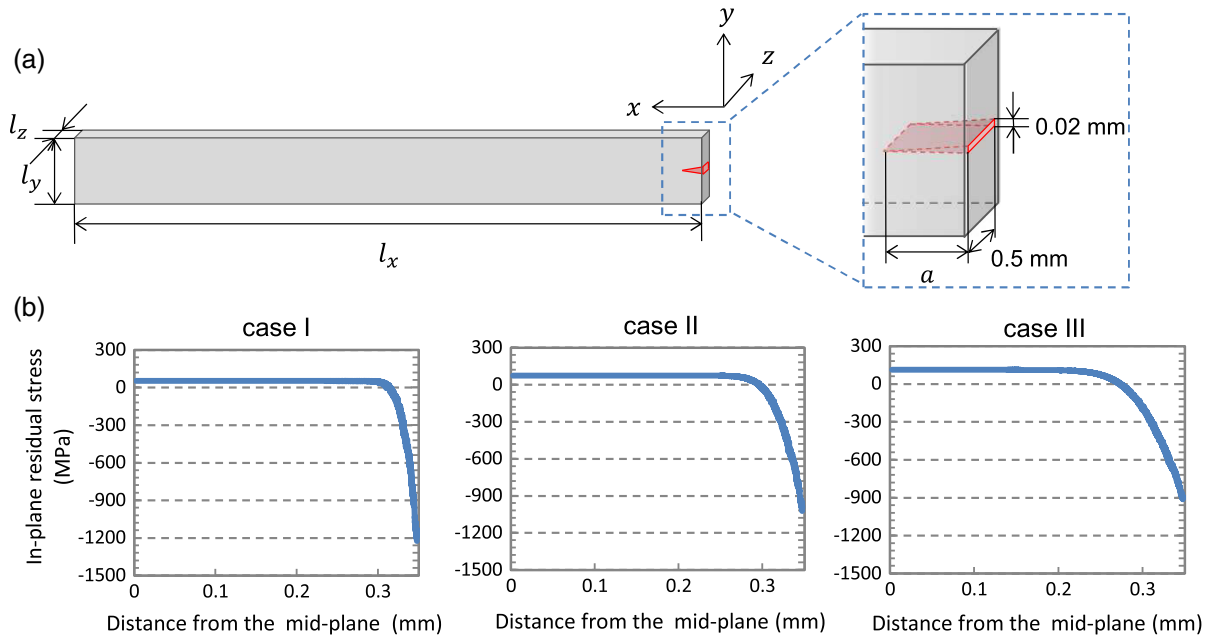


FIG. 1. Geometry of the analysis model and residual stress profiles of each analysis model. (a) Geometry of the analysis model with the initial crack. $l_x \times l_y \times l_z = 30 \times 2.0 \times 0.70$ mm. The initial crack is indicated by the red (dark gray) area. All the Voronoi boundaries in the initial crack area are fractured at $t = 0.0$ s. (b) The in-plane residual stress profiles (i.e., σ_{xx} or σ_{yy}) in the z direction for each analysis model. The horizontal axis shows the distance from the midplane (i.e., $z = l_z/2$ plane) in the z direction. The in-plane residual stress profile is symmetrical with respect to the midplane in the z direction.

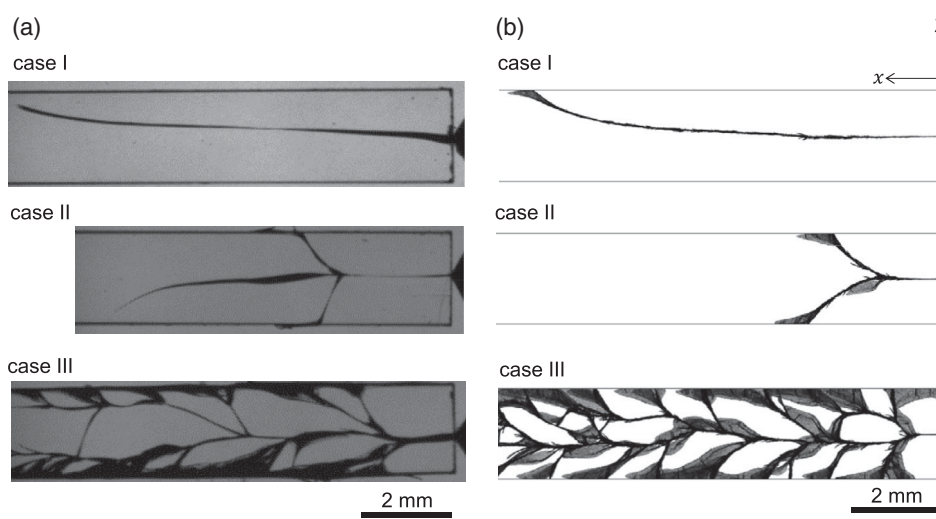


FIG. 2. Crack patterns of the chemically tempered glass sheets. (a) Crack patterns in the experiments. The width of the field of view of the experiments is about 8–10 mm from the impact surface. (b) Crack patterns in the numerical analyses. These snapshots trim off the area of $x > 10$ mm.

the crack velocity rapidly decreases near or below 2000 m/s. The experiments [Fig. 3(a)] and the numerical analyses [Fig. 3(b)] show perfect agreement in all these characteristics of the crack velocity.

Figures 4(a)–4(c) show the time history of the residual stress field at the midplane in the thickness direction obtained by the numerical analyses. The elastic wave generated by the fracture propagates antecedent to the crack tip. Also, the stress concentrates at the crack tips

and is released around the cracks. Contrary to the external applied loading, the distributed internal force due to inhomogeneous inelastic strain keeps acting on every local area even after fracture. This remaining internal force causes repetitive branching and catastrophic failure as seen in case III. The remaining residual stress in the isolated fragments forms a concentric distribution in each fragment. The residual stress distribution of the fragments and the release and the redistribution process of the residual stress

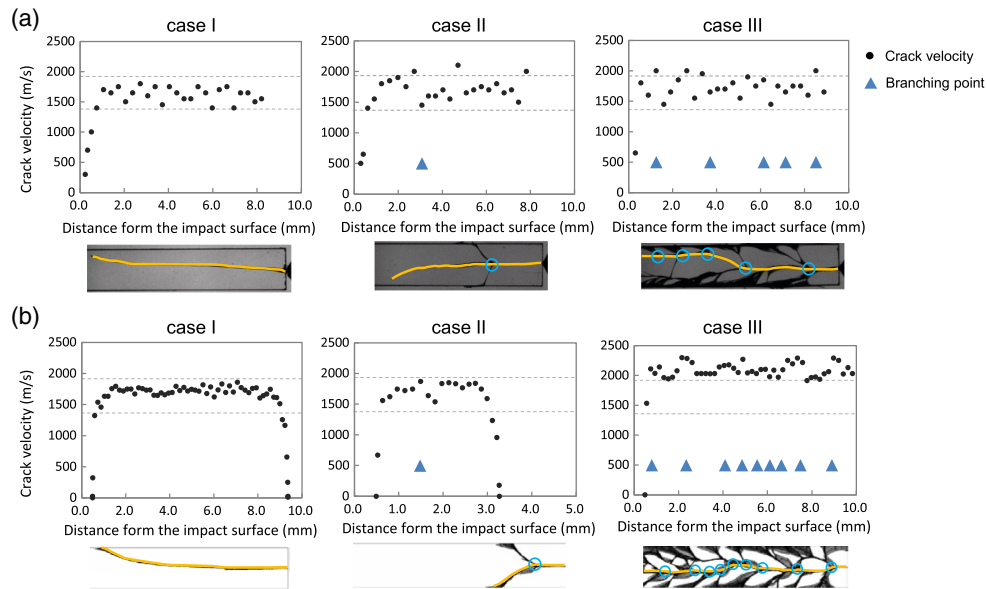


FIG. 3. Crack velocity vs distance from the impact surface with branching points. The positions of the branching points are indicated by the blue triangles. The crack velocity and the branching points were measured on the main crack in the field of view. The yellow (light gray) lines and the blue circles on the images of the crack patterns placed below each graph respectively show the main crack and the crack branching points used for the measurement. (a) Experiments. (b) Numerical analyses.

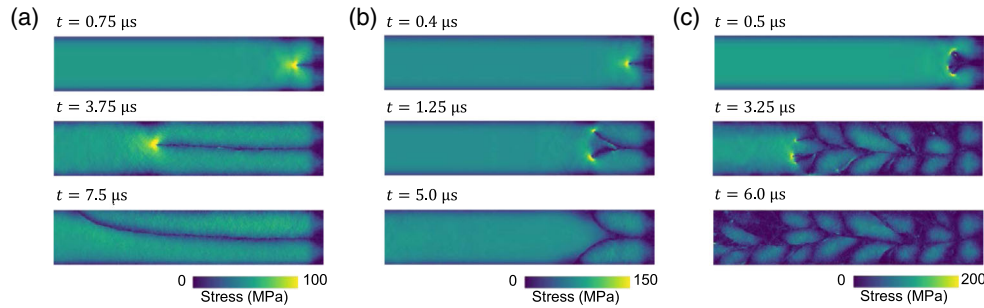


FIG. 4. Snapshots of the contours of the maximum principal stress at the midplane in the thickness direction obtained by numerical analyses. (a) Case I. (b) Case II. (c) Case III.

field during fracture cannot be captured by experimental methods. This is why numerical analysis is essential for fully understanding the crack propagation in a residual stress field.

Discussion.—We proposed a mathematical model and numerical analysis method for dynamic crack propagation in a residual stress field. Our model and method are validated through fracture experiments of the chemically tempered glass sheets. The fracture patterns and fracture processes depending on the residual stress profiles are perfectly reproduced by numerical analyses. Also, the crack velocity and the critical velocity for crack branching given by the numerical analyses coincide with the experimental observations. These results show that our model completely captures the mechanism for the dynamic fracture in a residual stress field. Our model suggests that the distributed internal force due to the inhomogeneous inelastic deformation plays a significant role in the dynamic fracture. This force keeps acting on every local area even in isolated fragments and thereby causes catastrophic fragmentation particularly observed in a residual stress field. Regardless of the source of the residual stress, this model is widely applicable to the dynamic fracture in a residual stress field. In addition, we visualized the process of the release and redistribution of the residual stress by numerical analyses, which are unobservable in experiments. This visualization will help us understand the change in the residual stress field and design the residual stress profile for industrial applications. We anticipate that the proposed model and method to be a general framework for quantitative evaluation and prediction for the dynamic fracture in a residual stress field.

This work was partially supported by JSPS KAKENHI Grant No. JP20K14812. S. H. and K. O. are the first authors of this Letter and contributed equally. S. H. and K. O. jointly conceived and developed the theory, wrote the computer codes, and wrote the manuscript. K. I. designed and directed the experimental part of the work and H. A. conducted the experiments. S. U. and Y. K. jointly designed the framework of the project and supported the interpretation of the data.

*hirobes@jamstec.go.jp

†ogunik@jamstec.go.jp

- [1] M. M. Chaudhri and C. Liangyi, The catastrophic failure of thermally tempered glass caused by small-particle impact, *Nature (London)* **320**, 48 (1986).
- [2] J. H. Nielsen, J. F. Olesen, and H. Stang, The fracture process of tempered soda-lime-silica glass, *Exp. Mech.* **49**, 855 (2009).
- [3] D. Y. Jang, T. R. Watkins, K. J. Kozaczek, C. R. Hubbard, and O. B. Cavin, Surface residual stresses in machined austenitic stainless steel, *Wear* **194**, 168 (1996).
- [4] M. A. S. Torres and H. J. C. Voorwald, An evaluation of shot peening, residual stress and stress relaxation on the fatigue life of AISI 4340 steel, *International Journal of Fatigue* **24**, 877 (2002).
- [5] J. H. Nielsen, Remaining stress-state and strain-energy in tempered glass fragments, *Glass Struct. Eng.* **2**, 45 (2017).
- [6] R. Harilal, C. P. Vyasrayani, and M. Ramji, A linear least squares approach for evaluation of crack tip stress field parameters using DIC, *Opt. Lasers Eng.* **75**, 95 (2015).
- [7] H. B. Zeng and P. Bailly, Experimental characterization of dynamic behavior of gelatin-based material using DIC, *Polymer Testing* **63**, 298 (2017).
- [8] M. Rossi, L. Cortese, K. Genovese, A. Lattanzi, F. Nalli, and F. Pierron, Evaluation of volume deformation from surface DIC measurement, *Exp. Mech.* **58**, 1181 (2018).
- [9] K. Takahashi, S. I. Aratani, and Y. Yamauchi, Dynamic fracture in zone-tempered glasses observed by high-speed photoelastic colour photography, *J. Mater. Sci. Lett.* **11**, 15 (1992).
- [10] M. L. L. Wijerathne, K. Oguni, and M. Hori, Tensor field tomography based on 3D photoelasticity, *Mech. Mater.* **34**, 533 (2002).
- [11] M. L. L. Wijerathne, K. Oguni, and M. Hori, Stress field tomography based on 3D photoelasticity, *J. Mech. Phys. Solids* **56**, 1065 (2008).
- [12] H. Aben, J. Anton, M. Paemurru, and M. Öis, A new method for tempering stress measurement in glass panels, *Est. J. Eng.* **19**, 292 (2013).
- [13] S. Aratani, Estimation of the stress σ_{CR} generated at propagating crack front, *J. Ceram. Soc. Jpn.* **126**, 246 (2018).
- [14] R. Dugnani, R. J. Zednik, and P. Verghese, Analytical model of dynamic crack evolution in tempered and strengthened glass plates, *Int. J. Fract.* **190**, 75 (2014).

- [15] M. Corrado and J. F. Molinari, Effects of residual stresses on the tensile fatigue behavior of concrete, *Cement and Concrete Research* **89**, 206 (2016).
- [16] J. H. Nielsen and M. Bjarrum, Deformations and strain energy in fragments of tempered glass: Experimental and numerical investigation, *Glass Struct. Eng.* **2**, 133 (2017).
- [17] M. Nose, H. Amano, H. Okada, Y. Yusa, and A. Maekawa, Computational crack propagation analysis with consideration of weld residual stresses, *Eng. Fract. Mech.* **182**, 708 (2017).
- [18] M. Hori, K. Oguni, and H. Sakaguchi, Proposal of FEM implemented with particle discretization for analysis of failure phenomenon, *J. Mech. Phys. Solids* **53**, 681 (2005).
- [19] K. Oguni, M. L. L. Wijerathne, T. Okinaka, and M. Hori, Crack propagation analysis using PDS-FEM and comparison with fracture experiment, *Mech. Mater.* **41**, 1242 (2009).
- [20] M. L. L. Wijerathne, K. Oguni, and M. Hori, Numerical analysis of growing crack problems using particle discretization scheme, *Int. J. Numer. Methods Eng.* **80**, 46 (2009).
- [21] S. Hirobe and K. Oguni, Coupling analysis of pattern formation in desiccation cracks, *Comput. Methods Appl. Mech. Eng.* **307**, 470 (2016).
- [22] S. Hirobe and K. Oguni, Modeling and numerical investigations for hierarchical pattern formation in desiccation cracking, *Physica (Amsterdam)* **359D**, 29 (2017).
- [23] A. A. Griffith, The phenomena of rupture and flow in solids, *Philos. Trans. R. Soc.* **221**, 163 (1921).
- [24] S. Hirobe, K. Imakita, H. Aizawa, Y. Kato, S. Urata, and K. Oguni, companion paper, Mathematical model and numerical analysis method for dynamic fracture in a residual stress field, *Phys. Rev. E*, **104**, 025001 (2021).
- [25] S. Karlsson, B. Jonson, and C. Stålhandske, The technology of chemical glass strengthening—A review, *Glass Technol.: Eur. J. Glass Sci. Technol. A* **51**, 41 (2010), https://www.researchgate.net/publication/233704764_The_Technology_of_A_Review.
- [26] A. K. Varshneya, Chemical strengthening of glass: Lessons learned and yet to be learned, *Int. J. Appl. Glass Sci.* **1**, 131 (2010).
- [27] G. Macrelli, Chemically strengthened glass by ion exchange: Strength evaluation, *Int. J. Appl. Glass Sci.* **9**, 156 (2018).
- [28] L. Casetti, Efficient symplectic algorithms for numerical simulations of Hamiltonian flows, *Phys. Scr.* **51**, 29 (1995).